Microneedle-Mediated Delivery of Lipid-Coated Cisplatin Nanoparticles for Efficient and Safe Cancer Therapy

Xinmiao Lan[1], Juncong She[2], Di-an Lin[2], Yu Xu[3], Xuan Li[4], Wei-fa Yang[1], Vivian Wai Yan Lui[5], Lijian Jin[4], Xi Xie[2,6], Yu-xiong Su[1,*]*

1. Discipline of Oral and Maxillofacial Surgery, Faculty of Dentistry, The University of Hong Kong, Hong Kong SAR, China
2. State Key Laboratory of Optoelectronic Materials and Technologies, School of Electronics and Information Technology; Guangdong Province Key Laboratory of Display Material and Technology, Sun Yat-Sen University, Guangzhou, China
3. School of Chinese Medicine, Li Ka Shing Faculty of Medicine, The University of Hong Kong, Hong Kong SAR, China
4. Discipline of Periodontology, Faculty of Dentistry, The University of Hong Kong, Hong Kong SAR, China
5. School of Biomedical Sciences, Faculty of Medicine, The Chinese University of Hong Kong, Hong Kong S.A.R., China
6. The First Affiliated Hospital of Sun Yat-Sen University, Guangzhou, China

[*]Corresponding author

Email: Yu-xiong Su: richsu@hku.hk; Xi Xie: xiexi27@mail.sysu.edu.cn

Abstract

Cisplatin is the first-line chemotherapeutic agent, but its systemic toxicity and side effects severely limit its clinical use. We report a microneedle technique to mediate the transdermal delivery of lipid-coated cisplatin nanoparticles (LCC-NPs) for efficient and safe cancer therapy. Cisplatin was encapsulated by tumor-targeting pH-responsive lipid nanoparticles with a high loading rate of 80%, and the encapsulation substantially increased the solubility of cisplatin and enhanced its antitumor efficiency *in vitro*. The LCC-NPs were embedded in dissolvable microneedles, and released from the microneedles after insertion into the skin. This enabled the nanoparticles to pass the stratum corneum for safe local delivery. An *in vivo* study with a xenograft tumor animal model demonstrated that microneedle arrays loaded with cisplatin nanoparticles significantly increased cytotoxicity and apoptosis in cancer cells with an apoptotic index of 58.6%, resulting in significantly reduced tumor volume and weight. Moreover, serum platinum, pulmonary toxicity, hepatotoxicity, and nephrotoxicity were not detected *in vivo*, indicating that this technique is bio-safe. The cisplatin-nanoparticle microneedle system developed in this study may offer promising opportunities in cancer therapy to enhance antitumor effects and reduce systemic toxicity and side effects.

Keywords: Cisplatin, Nanoparticle, Microneedle, Cancer therapy, Drug delivery

1. Introduction

Head and neck cancer is the sixth most common cancer worldwide, with only a 50% 5-year survival rate.[1] Despite of emerging research on new treatment strategies, chemotherapy remains one of the most important therapeutic modalities for cancers. Cisplatin (CDDP) is the most widely used DNA-modifying chemotherapeutic drug, which inhibits tumor growth by inducing apoptosis of cancer cells.[2] Various nanomaterials have been applied as drug vehicles[3-

[4] to enhance the therapeutic efficacy of CDDP and its bioavailability. Although both organic and inorganic materials have been used to fabricate nanoparticles to encapsulate CDDP,[4-6] organic materials such as solid lipids and polymers have exhibited unique advantages over organic materials, including biocompatibility and high drug-loading rates.[7] Depending on the mechanism, drug molecules can be encapsulated in the lipid or polymer core or adsorbed on the nanoparticle surface.[5, 8] Moreover, these nanoparticles have a relatively high drug loading ratio and reduced surface moisture loss.[9] The nanoparticles can release drug molecules in a burst or prolonged mode, and the drug release can be well tuned through manipulation of the composition or structure of the nanoparticles.[10]

CDDP is generally administered intravenously as a short-term infusion in saline for the treatment of solid malignancies. However, systemic administration of CDDP may cause severe side effects, such as nephrotoxicity, neurotoxicity, nausea and vomiting, ototoxicity, electrolyte disturbance, and hemolytic anemia [11]. Local transdermal delivery of CDDP or CDDP-encapsulated nanoparticles prevents systemic toxic effects. However, challenges remain in the transdermal delivery of CDDP and CDDP-encapsulated nanoparticles through topical applications because the corneum layers of the epithelia (e.g., skin and gum) act as a natural barrier preventing the penetration of nanoparticles. Transdermal injections of CDDP at the tumor site with conventional metal needles might cause skin necrosis and tumor spreading. Little progress has been achieved regarding the treatment of tumors through local application of CDDP. Therefore, an effective local delivery system for CDDP that combines high anticancer efficiency with low drug toxicity is required.

The recently developed microneedle (MN) technique offers a convenient and minimally invasive approach to transdermal drug delivery.[12-13] MNs are generally applied to penetrate the stratum corneum, thereby enabling skin-impermeable drugs to pass through the stratum corneum. The length of an MN is specifically designed to be sufficiently short, without harming the nerves or blood vessels in the dermis. MNs-mediated drug delivery has achieved great success in *in vivo* animal models in the fields for vaccination, obesity, diabetes, and acne vulgaris treatments.[14-20] Since 2016, MNs have been explored as an effective and minimally invasive tool for treatment of superficial tumors in animal models. For example, MN-mediated therapy completely eradicated 4T1 breast tumors in mice through combined application of photosensitive nanomaterials and the anticancer drug doxorubicin.[21] Hao et al. reported that near-infrared-responsive PEGylated-gold-nanorod-coated MNs enhanced the antitumor efficacy of docetaxel in an A431 tumor xenograft model.[22] In addition, MN-assisted delivery of immunotherapeutic agents has yielded satisfactory treatment outcomes in melanoma murine models.[23-25]

In this study, we demonstrated cancer therapy with high efficiency and safety through MN-mediated transdermal delivery of lipid-coated CDDP nanoparticles (LCC-NPs). Encapsulation of CDDP with lipid nanoparticles effectively regulated the release of CDDP and significantly reduced non-specific drug toxicity, and MNs enabled safe and effective transdermal delivery of the drugs to the local tumor site. The CDDP was effectively encapsulated in the lipid nanoparticles through reverse-phase microemulsion, which provided increased cellular uptake and enhanced cytotoxicity to cancer cells. LCC-NPs were loaded in MNs through the molding method; the MN-mediated local delivery of LCC-NPs significantly improved antitumor effects in a xenograft animal model of head and neck cancer, and systemic toxicity and side effects were minimized. This research provides a unique strategy to effectively and safely manage life-

threatening carcinoma through local applications of anti-tumor drugs, thereby avoiding the systemic toxic effects of current chemotherapy approches.

2. Results and Discussion

2.1 Characterization of LCC-NPs

CDDP is the first-line chemotherapy drug for head and neck squamous cell carcinoma (HNSCC). Studies have reported that nanoparticles greatly enhance therapeutic efficiency as drug vehicles for cancer treatment. However, the poor solubility of CDDP either in water or organic solvent inhibits its encapsulation into nanoparticles. In this study, *cis*-$[Pt(NH_3)_2(H_2O)_2]_2(NO_3)_2$ as the precursor of CDDP was applied to increase the drug solubility, while 1,2-dioleoyl-sn-glycerol-3-phospate (DOPA), 1,2-dioleoyl-3-trimethy-lammonium-propane (DOTAP), 1,2-distearoyl-sn-glycero-3-phosphoethanolamine-N-[amino(polyethylene glycol)-2000] (ammonium salt) (DSPE-PEG-AA), and cholesterol were selected to fabricate the LCC-NPs. Transmission electron microscopy (TEM) revealed that the as-prepared nanoparticles exhibited uniform sizes with a diameter of approximately 60 nm (Figure 1A); the average diameter measured using dynamic light scattering (DLS) was 63.6 nm ± 15.2 nm (Figure 1B). Because DOTAP, DSPE-PEG-AA, and cholesterol were distributed on the outer layers of the LCC-NPs, the resultant particle zeta potential was +12.8 mV, which yielded a good dispersion capacity of LCC-NPs in aqueous solutions. The selected DOPA was reported to control nanoparticle size and prevent aggregation.[10] Moreover, DOPA-encapsulated CDDP nanoparticles can be further dispersed in aqueous solution to form an outer coating bilayer by adding other lipids (i.e., DOTAP, DSPE-PEG-AA, and cholesterol). Among these, DOTAP can assist the escape of nanoparticles from the endosomes and reduce their accumulation in the lysosomes, whereas cholesterol can enhance selectivity to the target tumor and reduce

nephrotoxicity.[26] Notably, DSPE-PEG-AA labeling enables nanoparticles to target cancer cells because the anisamide in DSPE-PEG-AA can bind with the sigma receptors that are overexpressed in most human tumors.[27] Therefore, fabricated lipid nanoparticles can achieve a stable morphology and dispersion together with a cancer targeting effect.

Based on inductively coupled plasma optical emission spectrometry (ICP-OES) analysis, the drug-loading efficiency of the LCC-NPs was 80.0% ± 1.2%, which was significantly higher than those of other nanoparticles, such as mesoporous silica and hydroxyapatite nanoparticles.[28] To assess the sustained release of CDDP from nanoparticles, LCC-NPs were dialyzed in phosphate-buffered saline (PBS) under various pH conditions (4.1 and 7.4) for 72 h. The amount of CDDP released was determined by measuring the platinum (Pt) concentration through ICP-OES. No burst release was observed during the 72 h for either condition (Figure 1C). More CDDP was released in the acidic environment, indicating that the the synthesized LCC-NPs were pH sensitive. This is highly preferred for anti-cancer treatment due to the increased releasing amount of CDDP from the LCC-NPs in an acidic tumor microenvironment.

2.2 Enhanced in vitro anti-cancer effect of LCC NPs against HNSCC cell lines

2.2.1 Cytotoxicity and Cellular Uptake of LCC NPs

The cytotoxicity of LCC-NPs in three HNSCC cell lines (i.e., CAL 27, FaDu, SCC 15) was evaluated by cell counting kit 8 (CCK-8) and then assessed using half-maximal inhibitory concentration (IC_{50}) to show the anticancer efficiency *in vitro*. For all three cell lines, the IC_{50} values of the LCC-NPs were significantly lower than those of free CDDP (Figure 2A), indicating a higher drug efficiency after lipid coating and nanoencapsulation. Moreover, after the treatment (LCC-NPs vs. free CDDP) with the same Pt concentration, higher Pt uptake was

detected in the cell lines treated with LCC-NPs than in those treated with free CDDP (Figure 2B). Taken together, lipid coating and nanoencapsulation substantially increased the Pt uptake and eventually enhanced the anti-cancer effect of CDDP. The poor solubility of CDDP was reported to severely limit its bioavailability.[2] Thus, nanoencapsulation was proposed as an alternative approach to tackle this problem.

To demonstrate the subcellular localization of LCC-NPs, they were first labelled with 1,2-distearoyl-sn-glycero-3-phosphoethanolamine-N-[amino(polyethylene glycol)-2000] (ammonium salt) (NBD-PE) with green fluorescence and then treated with the cells for 4 h. As shown in Figure 2C, most LCC-NPs appeared in the cytoplasm and a few were trapped in lysosomes stained with LysoTracker red showing the overlapped yellow color. This trapping was due to the incorporation of DOTAP on the nanoparticle surface, which induced the endosomal escape of the nanoparticles and prevented drug degradation by the lysosome. The degradation of LCC-NPs in the cytoplasm caused intracellular CDDP release, leading to the cell death *in vitro*. This may also contribute to the higher cytotoxicity of LCC-NPs to cancer cells.

2.2.2 Cell Apoptosis and Cell Cycle arresting

The mechanism of anti-cancer effect was studied by investigating the cell apoptosis and cell cycle arresting after the 4 h treatment of free CDDP or LCC-NPs. Cell apoptosis was detected through both flow cytometry and *in situ* fluorescence imaging. The apoptotic cells were stained with annexin V conjugated to green fluorescent Fluorescein isothiocyanate (FITC) dye, while necrotic cells were stained with propidium iodide (PI). Annexin V conjugates are useful for detecting translocated phosphatidylserine, a hallmark of apoptosis. Referring to cell apoptosis,

quantitative flow cytometry measurements showed that the percentages of FaDu cells undergoing apoptosis in control, free CDDP, and LCC NPs treated groups were 0.27%, 38.3%, and 50.7%, respectively (Figure 2D). Furthermore, apoptotic DNA fragmentation in the cells was assessed through terminal deoxynucleotidyl transferase dUTP nick end labeling (TUNEL) assay followed by fluorescence imaging. More green-colored apoptotic FaDu cells were found in LCC-NPs treated group (55.4%) than in the CDDP treated group (33.3%) (Figure 2E). Similar patterns were also observed in CAL 27 and SCC 15 cells (Figures S1 and S2). These results further demonstrated the enhanced drug efficiency of CDDP after lipid coating and nanoencapsulation. Moreover, the flow cytometry measurements revealed that cell cycles of FaDu, CAL 27, and SCC 15 cells treated with CDDP and LCC-NPs was arrested in the G1 phase (Figures 2F, S1 and S2). LCC-NPs arrested the cell cycle at the DNA pre-synthetic gap (G1) phase and caused more cell apoptosis than did free CDDP, suggesting higher anti-cancer efficiency of LCC-NPs.

2.3 Characterization of Dissolvable MNs

To enable transdermal delivery of the LCC-NPs, dissolvable MNs were utilized to further encapsulate LCC-NPs for delivery through skin. Fabrication and encapsulation of LCC-NPs were achieved through a molding method (Figure 3A). As shown in scanning electron microscope (SEM) images (Figure 3B and C), the fabricated MN patch consisted of 81 (9 × 9) needles with lengths of approximately 800 μm and base diameters of approximately 400 μm. The MN tips could be dissolved completely within 5 min in water (Figure S3), indicating a good solubility. To observe the loading of LCC-NPs in MNs, nanoparticles were labeled with NBD-PE (green fluorescence) and imaged using fluorescence microscopy (Figure 3D) and confocal fluorescence microscopy (Figure 3E). The confocal laser scanning microscope (CLSM) images showed that the fluorescent NPs were uniformly distributed on the MN tips.

Furthermore, a skin insertion test was performed on porcine skin (Figure 3F) to investigate the insertion ability. The MN patch was pressed against the porcine skin for 5 min, which was rapidly dissolved after insertion, as shown in the SEM images in Figure 3G,H. CLSM imaging revealed that the fluorescent nanoparticles were deposited in the skin tissue in an array profile (Figure 3I). These results suggested that MNs enabled effective transdermal delivery of LCC-NPs. To examine the stability of LCC-NPs loaded in MNs, the MNs containing LCC-NPs were stored at room temperature for 3 months. The MNs were then dissolved in cell culture medium to release the LCC-NPs and the cytotoxicity of LCC-NPs to HNSCC cell lines were measured. The induced IC_{50} did not show significant difference ($p>0.05$) compared with the IC_{50} values induced by fresh-prepared drugs (Figure S4), indicating that the LCC-NPs in MNs maintained stability when stored at room temperature. Moreover, the MN material, sodium carboxymethycellulose (SCMC), did not induce significant cellular cytotoxicity (Figure S5), indicating the safety of the MN material.

2.4 MNs Enhance Antitumor Effects and Reduce Systemic Toxicity and Side Effects

2.4.1 In Vivo Antitumor Outcome

The antitumor efficiency of MNs-mediated delivery of LCC-NPs was investigated in a xenograft head and neck tumor model using FaDu cells[29-30] (Figure 4A). Tumor volume and weight were compared among different groups (Figures 4B–D), including (i) blank control, (ii) intravenous (i.v.) injection with solution of free CDDP (indicated as CDDP), (iii) i.v. injection with LCC-NPs (indicated as LCC-NPs), (iv) local subcutaneous (s.c.) injection with solution of free CDDP (indicated as CDDP locally), (v) CDDP-loaded MNs (indicated as CDDP MNs), (vi) LCC-NPsloaded MNs (indicated as LCC-NPs MNs). Mice injected with saline exhibited natural tumor growth, and tumor proliferation was somewhtat inhibited in mice who received

i.v. injection and s.c. injections of drugs. Among the three groups, the LCC-NPs exhibited the most apparent inhibition of tumor growth, indicating that LCC-NPs can target the cancer cells to enhance antitumor efficiency. Because free drugs may be metabolized before they accumulate in tumor, a safe local drug delivery system is required. However, local s.c. injection of CDDP caused severe skin ulceration and necrosis (Figure 4A), which could hinder its clinical application in patients. By contrast, only two skin ulcers occurred in the CDDP MNs group, and only one mild skin ulcer occurred in the group who received MNs loaded with LCC-NPs. Therefore, LCC-NPs MNs could be a promising anti-tumor strategy without inducing skin damage. Meanwhile, both MNs groups showed significantly increased anticancer effects compared with other groups ($p < 0.05$). LCC-NPs MNs improved treatment outcomes compared to CDDP MNs, although the differences were not statistically significant ($p > 0.05$). These results indicated LCC-NPs loaded MNs represent a safe and efficient transdermal delivery system for chemotherapy with improved antitumor outcomes.

2.4.2 Tumor Cell Apoptosis and Proliferation In Vivo

To further elucidate the histopathological mechanism of the antitumor effects *in vivo*, TUNEL assay was used to detect cell apoptosis, and Ki-67 Immunohistochemistry (IHC) was conducted to detect cell proliferation in formalin-fixed paraffin-embedded tumor tissue sections. Representative images are shown in Figure 5. Ki-67 IHC revealed a decrease in cell proliferation that was more marked in the MNs groups than in the other groups ($p < 0.05$). More than 60% of the cells in the control group continued proliferating, whereas the corresponding rates were approximately 40% and 20% in the i.v. groups and MN groups, respectively. These results suggested that LCC-NPs MNs have great potential to inhibit cancer cell proliferation. Similarly, TUNEL assay revealed that more cell apoptosis was induced in

the MN groups ($p < 0.05$), whereas few apoptotic cells (less than 15%) were observed when free drug was administered systemically, and none were noted in the control group. LCC-NPs induced more tumor regression than did free CDDP both *in vitro* and *in vivo*. Specifically, the LCC-NP-coated MNs group produced more prominent effects than the CDDP MNs group did, and the differences were statistically significant ($p < 0.05$). These data confirmed that LCC-NPs MNs effectively inhibit tumor cell proliferation and promote apoptosis *in vivo*.

2.4.3 Systemic Toxicity and Side Effects

Systemic toxicity and side effects are major clinical limitations of CDDP and lead to impaired tolerability and poor compliance among cancer patients. This can adversely affect the cancer treatment outcome. As is shown in Figure 6A, i.v. CDDP caused significantly greater loss in body weight than did the other treatment methods. Notably, only the LCC-NPs MN groups exhibited weight growth trends, whereas weight loss was observed in the control and CDDP MN groups 3 days after the final injection. This finding was interesting and important. Cancer can cause considerable weight loss and wasting, resulting in cancer cachexia.[31-32]Additionally, weight loss is also one of the major side effects of CDDP chemotherapy.[33] The weight loss observed in the control group was due to cancer cachexia, and both CDDP toxicity and cancer cachexia led to weight loss in other treatment groups. The body weight gain observed in the LCC-NPs MNs group not only demonstrated anticancer efficiency, which resulted in cancer cachexia being overcome, but also revealed the safety superiority of LCC-NPs MNs. To investigate the bio-distribution of the drugs in the circulation, the Pt serum concentration in serum was determined through ICP-OES. Both i.v. and s.c. injection of CDDP caused significant accumulation of Pt in serum, whereas reduced Pt serum concentration was observed after LCC-NPs-mediated targeted delivery (Figure 6B). Notably, no Pt was detected in the

control group or MNs groups, indicating that MNs-mediated local delivery could dramatically reduce the toxicity of chemotherapy drugs.

Immunoglobulin G (IgG), the most abundant antibody found in all body fluids, protects the body against bacterial and viral infections. Mouse total IgG in serum was determined after sacrifice (Figure 6C). MNs and control groups showed significantly higher total IgG compared with other groups, and the LCC-NPs MNs group exhibited the highest level, although no significant difference was detected between MNs and control groups. CDDP tends to accumulate in kidney, resulting in nephrotoxicity. Blood urea nitrogen (BUN) level represents kidney function with a normal from 12 to 33 mg/L. According to Figure 6 and Table 1, the BUN values in the control and MNs groups were within the normal range, whereas the values in the other three groups were higher than normal.

Nephrotoxicity, hepatotoxicity, and pulmonary toxicity are primary fatal complications of CDDP therapy. The lungs, livers, and kidneys were harvested after sacrifice and embedded in paraffin and stained with H&E (Figure 6E). In the i.v. CDDP group, diffused damage of pulmonary alveoli and severe inflammatory infiltration were observed in the lungs. Capillaries in the alveolar walls were dilated and congested with red blood cells in the CDDP local injection group. Other groups showed normal microscopic lung structures. In mice treated with systemic CDDP, microscopic view exhibited a feathery membrane of hepatic cells and cytoplasm. In the CDDP s.c. injection group, hepatic cells exhibited a foamy appearance and extensive dissolution of cytoplasm. In contrast, the LCC-NPs and MN groups showed generally normal structures with slight disintegration of the hepatic cords. Nephrotoxicity is the most serious side effect related to CDDP. As expected, in both CDDP groups, extensive nephron

damage was observed, with the glomeruli collapsed and mesangial cells fused with surrounding tubules. Arteries were dilated and filled with red blood cells. Specifically, the Bowman's capsule collapsed, and the Bowman's space disappeared in the CDDP systemic injection group, whereas scattered lymphocyte infiltration was observed in the local injection group. Remarkably, no nephrotoxicity was observed in the other groups. CDDP induced severe toxicity and side effects in organs, whereas LCC-NPs significantly reduced the toxicity. No obvious organ toxicity was observed in MNs groups. The *in vivo* study revealed encouraging findings that MNs greatly reduced the toxicity and side effects of CDDP. This may substantially improve patient tolerability and result in improved treatment outcomes.

3. Conclusion

In summary, lipid coating and nanoencapsulation increased the solubility and drug efficiency of CDDP, and MNs enabled further enhancement of the anti-cancer effect and markedly reduced the systemic toxicity and side effects through transdermal delivery. LCC-NPs were internalized by the cancer cells and then escaped from the endosomes. Their degradation in the cytoplasm released CDDP intracellularly, leading to cell death *in vitro*. Moreover, MNs could mediate the transdermal delivery of LCC-NPs and enhance the anti-tumor effects by inducing more cell apoptosis and suppressing cancer cell proliferation *in vivo*. Taken together, MN-facilitated delivery of LCC-NPs may have promising clinical applications for the treatment of superficial carcinomas such as head and neck cancer.

4. Materials and Methods

4.1 Materials

CDDP (*cis*-Diammineplatinum (II) dichloride), cyclohexane, Igepal®-520, Triton™ X-100, hexanol, and silver nitrate were purchased from Sigma-Aldrich (St. Louis, MO, USA). The lipids, DOPA, DOTAP, NBD-PE, DSPE-PEG-AA, and cholesterol were obtained from Avanti Polar Lipids (Alabaster, AL, USA).

4.2 Cell Culture

HNSCC cell lines FaDu, CAL 27, and SCC 15, were cultured for the following procedures. All cell lines were obtained from the American Type Culture Collection (ATCC, Manassas, VA, USA). FaDu and CAL 27 were cultured in Dulbecco's Modified Eagle's Medium (Gibco, Gran Island, NY, USA) supplemented with 10% (V: V) fetal bovine serum (FBS, Gibco, USA) and 100 U/mL penicillin-streptomycin (Gibco, USA) in a humidified atmosphere with 5% CO_2 at 37 °C. SCC 15 was maintained in Dulbecco's Modified Eagle's Medium: Nutrient Mixture F-12 (Gibco, USA), with 10% FBS, 100 U/mL penicillin-streptomycin, and 400 ng/mL hydrocortisone (Sigma-Aldrich, USA) at 37 °C in a humidified atmosphere with 5% CO_2.

4.3 Synthesis of pH-Responsive Tumor-Targeting LCC-NPs

4.3.1 Synthesis of cis-$[Pt(NH_3)_2(H_2O)_2]_2(NO_3)_2$ Precursor

cis-$[Pt(NH_3)_2(H_2O)_2]_2(NO_3)_2$ was synthesized according to the literature.[34] To obtain a mixture, 0.2 mmol CDDP was dissolved in 1.0 mL deionized (DI) water, followed by the addition of 0.39 mmol silver nitrate. The mixture was subsequently heated at 60 °C for 3 h. After stirring overnight protected from light by aluminum foil, the solution was centrifuged at 16000 rpm for 15 min to remove silver chloride precipitate. The supernatant was filtered through a 0.22 μm

syringe filter. Subsequently, the concentration of Pt was determined through ICP-OES (Spectro Arcos, Kleve, Germany) and adjusted with water to a final concentration of 200 mM.

4.3.2 Preparation of LCC-NPs

LCC-NPs were prepared through reversed-phase microemulsion. The preparation procedure is briefly illustrated in graphic abstract. A solution composed of cyclohexane/Igepal® CO-520 (71%: 29%, V: V) and cyclohexane/Triton™ X-100/hexanol (75%: 15%: 10%, V: V: V) (3:1) was prepared. Subsequently, 800 mM KCl in water and 200 mM *cis*-$[Pt(NH_3)_2(H_2O)_2]_2(NO_3)_2$ were separately dispersed into the solution to form a well-dispersed, water-in-oil reverse microemulsion. After the same volume of DOPA (20 mM) was added to the precursor solution and stirred for 20 min, the two emulsions were mixed and stirred for another 30 min. Ethanol was added to the mixture, which was centrifuged at 12000 g for more than 15 min to remove the cyclohexane and surfactants. The particles were dispersed into chloroform after washing with ethanol three times. For the 1.0 mL LCC-NP cores, 50 μL of 20 mM DOTAP, 50 μL of 20 mM cholesterol, and 50 μL of 10 mM DSPE-PEG-AA were combined. After chloroform evaporation, the residual particles were dispersed in 1.0 mL of DI water.

4.3.3 Characterization of LCC-NPs

The LCC-NPs were stained with 2% uranyl acetate, and their morphology was observed through TEM (CM100, Philips Electron Optics, Eindhoven, Netherlands). The particle size and zeta potential were determined using a dynamic light scattering particle analyzer ((Nanotrac Wave II, Microtract, Montgomeryville, PA, USA). The concentration of Pt was detected through ICP-OES, and the drug loading capacity was determined using the Pt content.

4.3.4 In Vitro Drug Release

Weighed freeze-dried LCC-NPs were suspended in release medium and transferred into a dialysis bag (MWCO 3500 Da, ThermoFisher Scientific, Waltham, MA, USA). The nanoparticles were dialyzed against PBS buffer (pH = 4.1 and 7.4) at room temperature. Subsequently, 3 mL of the release solution was removed and replenished with an equal volume of fresh PBS at certain time points (6, 12, 24, 48, and 72 h). All the experiments were conducted three times. The released CDDP was examined by measuring Pt concentration in the collected solution through ICP-OES.

4.4 In Vitro Antitumor Study of LCC-NPs

4.4.1 Cell Toxicity

FaDu, CAL 27, and SCC 15 cell lines were seeded into a 96-well plate at a density of 1×10^4 cells per well and cultured for 24 h. The cells were treated with different concentrations of CDDP and LCC-NPs for another 24 h. The cell viability was determined using Cell Counting Kit-8 (CCK-8, Dojindo, Tokyo, Japan), whereas the half-maximal inhibitory concentration (IC_{50}) was calculated using SPSS software (v.24.0, IBM SPSS, Chicago, IL, USA).

4.4.2 Cellular Uptake

To assess the cellular uptake of LCC-NPs, FaDu, SCC 15, and CAL 27 cells were first seeded on round poly-D-lysine-coated coverslips. Cells were treated with CDDP or NBD-PE-labeled LCC-NPs at a concentration of 100 µM Pt at 37 °C for 4 h. The nuclei were stained with Hoechst 33342 (ThermoFisher Scientific, USA), and lysosomes were stained with lysotracker

red (ThermoFisher Scientific, USA). The fluorescence was visualized under a CLSM(FV1000, Olympus, Tokyo, Japan).

Cells were seeded in 24-well plates at a density of 5×10^5 cells per well and treated with CDDP and LCC-NPs with the same Pt concentration as mentioned previously. After 4 h of incubation, the cells were washed with PBS twice and digested in HNO_3 (69%). The digested system was then diluted with water to a final concentration of 2% HNO_3, and the Pt was measured through ICP-OES.

4.4.3 Cell Apoptosis and Cell Cycle

The three HNSCC cell lines were seeded in a six-well plate for flow cytometry, and cell apoptosis and cell cycle were analyzed. For terminal deoxynucleotidyl transferase dUTP nick end labeling (TUNEL, ThermoFisher Scientific, USA) assay, cells were seeded on 18-mm round poly-D-lysine-coated coverslips. All the cells were treated with CDDP or LCC-NPs at a concentration of 100 μM Pt at 37 °C for 4 h after attachment. For cell apoptosis and cell cycle analysis through fluorescence-activated cell sorting, cells were collected through trypsinization and stained with a Dead Cell Apoptosis Kit with Annexin V Alexa Fluor™ 488 and propidium iodide (ThermoFisher Scientific, USA) following the manufacturer's protocol. Cells were analyzed through flow cytometry immediately after staining (BD FACS CantoII Analyzer, BD, Franklin Lake, NJ, USA). For *in situ* cell apoptosis detection, cells on coverslips were fixed using 4.0% paraformaldehyde (PFA) and then stained with Click-iT™ TUNEL Alexa Fluor™ 488 Imaging Assay (ThermoFisher Scientific, USA) and Hoechst 33342 following the manufacturer's protocol. Then, the TUNEL-positive cells were counted under the CLSM.

4.5 Fabrication of dissolving MNs Coated with LCC-NPs

4.5.1 Fabrication and Characterization of MNs

Polydimethylsiloxane (PDMS) was used to prepare an inverted-cone-shaped mold for fabricating MNs. Subsequently, CDDP or LCC-NPs were dissolved in DI water supplemented with 8% SCMC. The solution was poured into the MN mold and centrifuged to drive the solution into the cone cavities, and excess solution was withdrawn. The PDMS mold with cavities filled with cellulose solution was dried at 40 °C for 2 h to form the MN tips. SCMC solution without CDDP or LCC-NPs was added into the mold, and dried at 40 °C for 2 h to form the MN patch base. The MNs were peeled off from the mold. NBD-PE was used to label nanoparticles with fluorescence during nanoparticle fabrication. The morphology of the MNs was observed through an SEM (SU1510, Hitachi, Tokyo, Japan). NBD-PE-labeled MNs were visualized under a CLSM.

To determine the toxicity of SCMC, three HNSCC cell lines were seeded on 96-well plates and separately treated with 0.6 μL of 0% (control group), 4%, 8%, 16%, and 32% SCMC in PBS. After 48 h, cell viability was analyzed using CCK-8 and calculated as the optical density (OD) of the treatment groups divided by that of the control group.

4.5.2 In Vitro Skin Insertion Test and Stability of MNs

NBD-PE-labeled dissolving MNs were inserted into porcine skin for 5 min and subsequently examined through a CLSM immediately. Both the surface of the porcine skin and the needles were imaged to analyze the insertion ability of the MNs.

Fabricated MNs could be stored in room temperature protected from light by aluminum foil. MNs were dissolved into cell culture medium to detect cytotoxicity and stability after 3 months. The three HNSCC cell lines were seeded in a 96-well plate and treated with different concentrations of dissolved MNs. Cell viability was analyzed using CCK-8.

4.6 In Vivo Study of MNs in a Xenograft Tumor Model

4.6.1 In Vivo Antitumor Efficacy Evaluation

Female BALB/c nude mice, 4-5 weeks old and 9 -12 g weight, were maintained in a pathogen-free facility (Lab animal unit, LAU, HKU). All of the animal procedures were performed in accordance with a protocol approved by the Committee on the Use of Live Animals in Teaching and Research (CULATR, HKU). A total of 1×10^6 FaDu cells suspended in 100μL Hanks' balanced salt solution (HBSS, Gibco, USA) were injected subcutaneously into right flank of mice. Tumors formulated one week after injection. Mice were randomly divided into six groups, as indicated in "2.4.1 *In vivo* antitumor outcome" All the treatments were given every 3 days for three cycles. 4.0 mg/kg Pt was administered for each mouse in the treatment groups. 0.12mg Pt was encapsulated in each microneedle. For MN groups, mice were anesthetized through intraperitoneal (*i.p.*) injection of ketamine hydrochloride (1.5 mg/kg; Alfasan International B.V., Woerden, Holland) and xylazine hydrochloride (0.2 ml/kg; Alfasan International B.V., Woerden, Holland) before applying MNs. Tumor growth and body weight were monitored. Tumor length and width were measured using calipers every 3 days. Tumor volume was calculated as: Tumor volume = $0.5a \times b^2$ (a: length, b: width). After sacrifice of the mice, the volume and wet weight of tumors were measured as well.

4.6.2 TUNEL Assay

Tumors were harvested after sacrifice and then fixed in 4% PFA and embedded in paraffin for the preparation of 5-μm-thick sections. TUNEL assay was performed according to the manufacturer's protocol. Cells with green-labeled nuclei were regarded as TUNEL-positive. TUNEL-positive cells were counted in three images at 4× magnification. The cell nuclei were stained with Hoechst 33342.

4.6.3 Detection of Ki-67

IHC was performed on selected slides from each tumor tissue. After deparaffinization and rehydration of the formalin-fixed paraffin-embedded tissue sections, antigen retrieval was performed for each section. The sections were incubated with rabbit anti-Ki-67 (Abcam, Cambridge, MA, USA) at 4 °C overnight, detected by a Rabbit Specific HRP/DAB Detection IHC Kit (Abcam, USA), and then counterstained with hematoxylin. Finally, tissues were examined through optical microscopy and photography (ECLIPSE LV100POL, Nikon, Tokyo, Japan), and images were analyzed using Image J software (NIH, Bethesda, MD, USA).

4.6.4 Pharmacokinetic Study

Mouse blood samples were collected before sacrifice. The collected blood samples were centrifuged, immediately frozen under liquid nitrogen, and stored at −80 °C until further assay. The serum was digested with 69% HNO_3 and diluted in water to a final concentration of 2%. The Pt concentration in serum was detected through ICP-OES.

4.6.5 Toxicity and Side Effects Study

The livers, kidneys, and lungs of mice were harvested after sacrifice. All tissues were fixed and embedded in paraffin. Hematoxylin and eosin (H&E) staining was performed. Images were collected using a polarized light microscope (ECLIPSE LV100POL, Japan). BUN in the serum was measured using a urea nitrogen detection kit (ThermoFisher Scientific, USA). Total IgG in serum was detected using a mouse IgG total ELISA kit (ThermoFisher Scientific, USA).

4.7 Statistical Analysis

Quantitative data are presented as mean ± standard derivation (SD). Data analyses of variance were performed in SPSS (v.24.0, IBM SPSS, USA) using one-way ANOVA, multiple *t* tests, or the Mann–Whitney *U* test. A p value < 0.05 was considered statistically significant.

Acknowledgement

The project was supported by Hong Kong Research Grant Council General Research Fund No. 17120718, HKU Seed Fund for Basic Research Nos. 201611159117 and 201511159130. Xi Xie would like to acknowledge financial support from the National Natural Science Foundation of China (Grant No.51705543, 61771498 and 31530023). Vivian Wai Yan Lui is funded by the Research Grant Council, Hong Kong (#17114814, #17121616, General Research Fund; and T12-401/13-R Theme-based Research Scheme), and the Hong Kong Cancer Fund, Hong Kong. We also appreciate HKU Li Ka Shing Faculty of Medicine Faculty Core Facility for the technical supports.

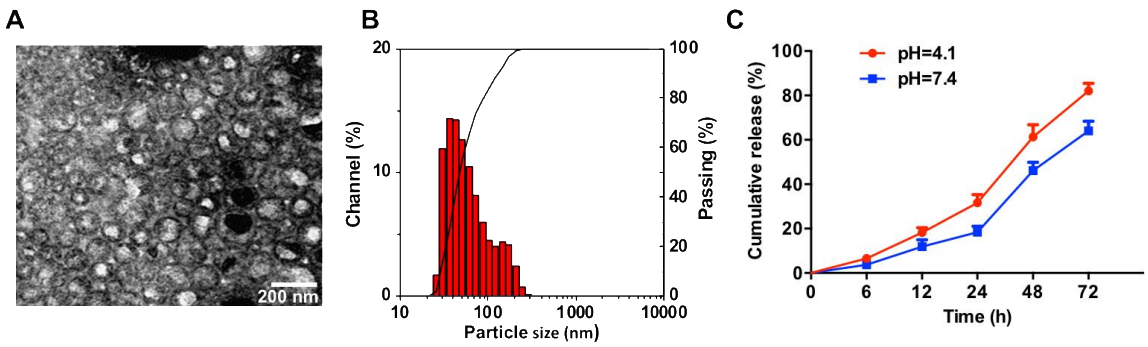

Figure 1. (A) Characterization of LCC-NPs: LCC-NP morphology imaged via TEM after staining with 2% uranyl acetate. Particles with white core and black border are LCC-NPs. (B) DLS studies showing particle size distribution of LCC-NPs (n = 3). (C) *In vitro* release of Pt from LCC-NPs in PBS of different pH values (n =3) (pH = 4.1, 7.4).

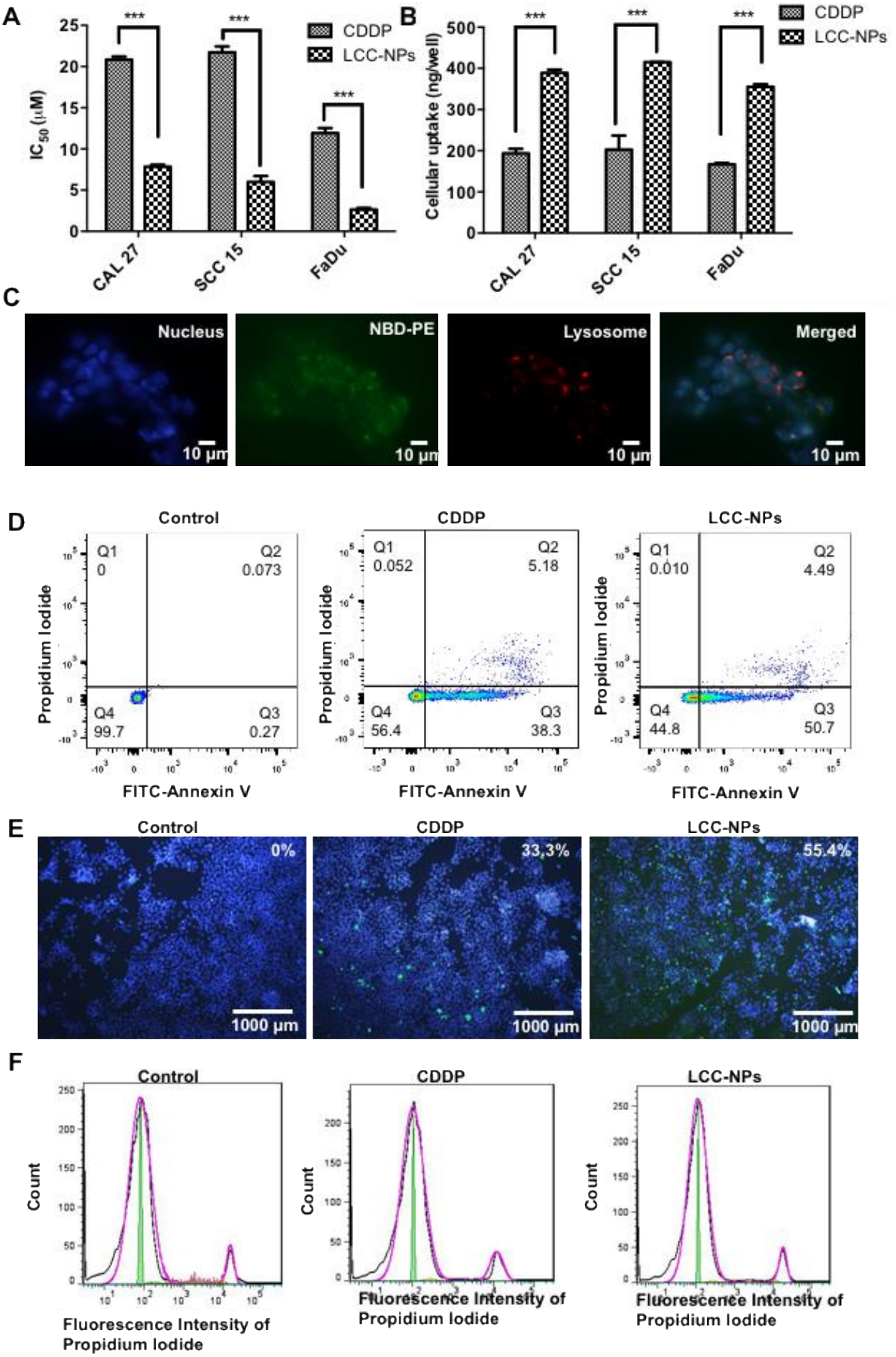
A
B
C
D
E
F
CDDP
LCC-NPs
IC50 (μM)
Cellular uptake (ng/well)
CAL 27
SCC 15
FaDu
***
Nucleus
NBD-PE
Lysosome
Merged
10 μm
Control
CDDP
LCC-NPs
Propidium Iodide
FITC-Annexin V
Q1
Q2
Q3
Q4
0
0.073
99.7
0.27
0.052
5.18
56.4
38.3
0.010
4.49
44.8
50.7
0%
33,3%
55.4%
1000 μm
Count
Fluorescence Intensity of Propidium Iodide

Figure 2. (A) IC_{50} of CDDP and LCC-NPs in three HNSCC cell lines (CAL 27, FaDu, and SCC 15); (B) CDDP or LCC-NPs uptake by three HNSCC cell lines; Cell uptake determined using Pt analyzed through ICP-OES: Cells were treated with these two drugs at a Pt concentration of 100 μM in a 24-well plate for 4 h. Each bar represents the mean ± SD of three independent experiments. Analysis of variance was conducted using one-way ANOVA was used (*** $p < 0.05$); (C) Cellular uptake of NBD-PE labeled LCC-NPs (green) and their subcellular localization in FaDu cells were imaged using fluorescence microscopy, and cell nuclei and lysosomes were stained with Hoechst 33342 (blue) and LysoTracker red, respectively; (D) After treatment with CDDP or LCC-NPs for 4 h, the apoptotic DNA fragmentation in the treated FaDu cells was studied using an *in situ* TUNEL assay followed by fluorescent imaging; (E) FaDu cells were stained with annexin V conjugated FITC and PI. The cell apoptosis was analyzed using flow cytometry; (F) Cell cycle distribution of the treated cells was evaluated using flow cytometry.

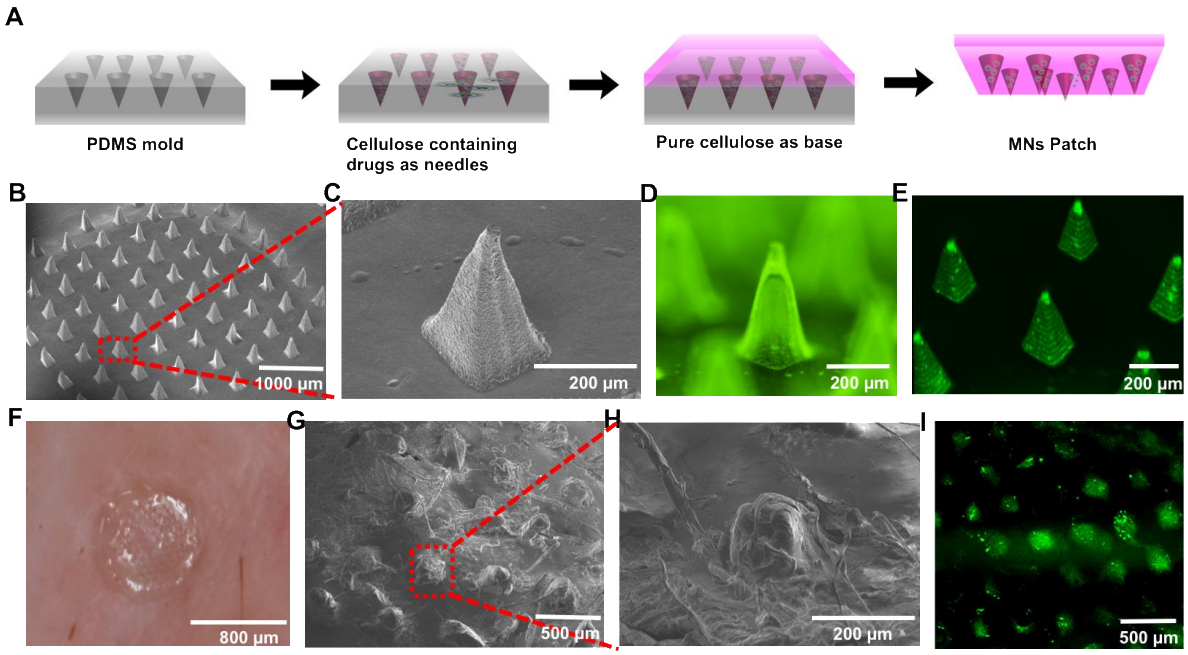

Figure 3. (A) Fabrication process of MNs. (B) SEM images of LCC-NP-coated MNs (C) Magnified SEM images of the MNs within the red box of (B). (D) Fluorescence microscope image. (E) Confocal image of NBD-PE-labeled NP-coated MNs. (F) Photograph of microneedle patch pressed into porcine skin. (G) SEM images of dissolved microneedle after inserting into skin. (H) Magnified SEM image of MNs in red box of (G). (I) Confocal image of porcine skin after treatment with NBD-PE-labeled MNs.

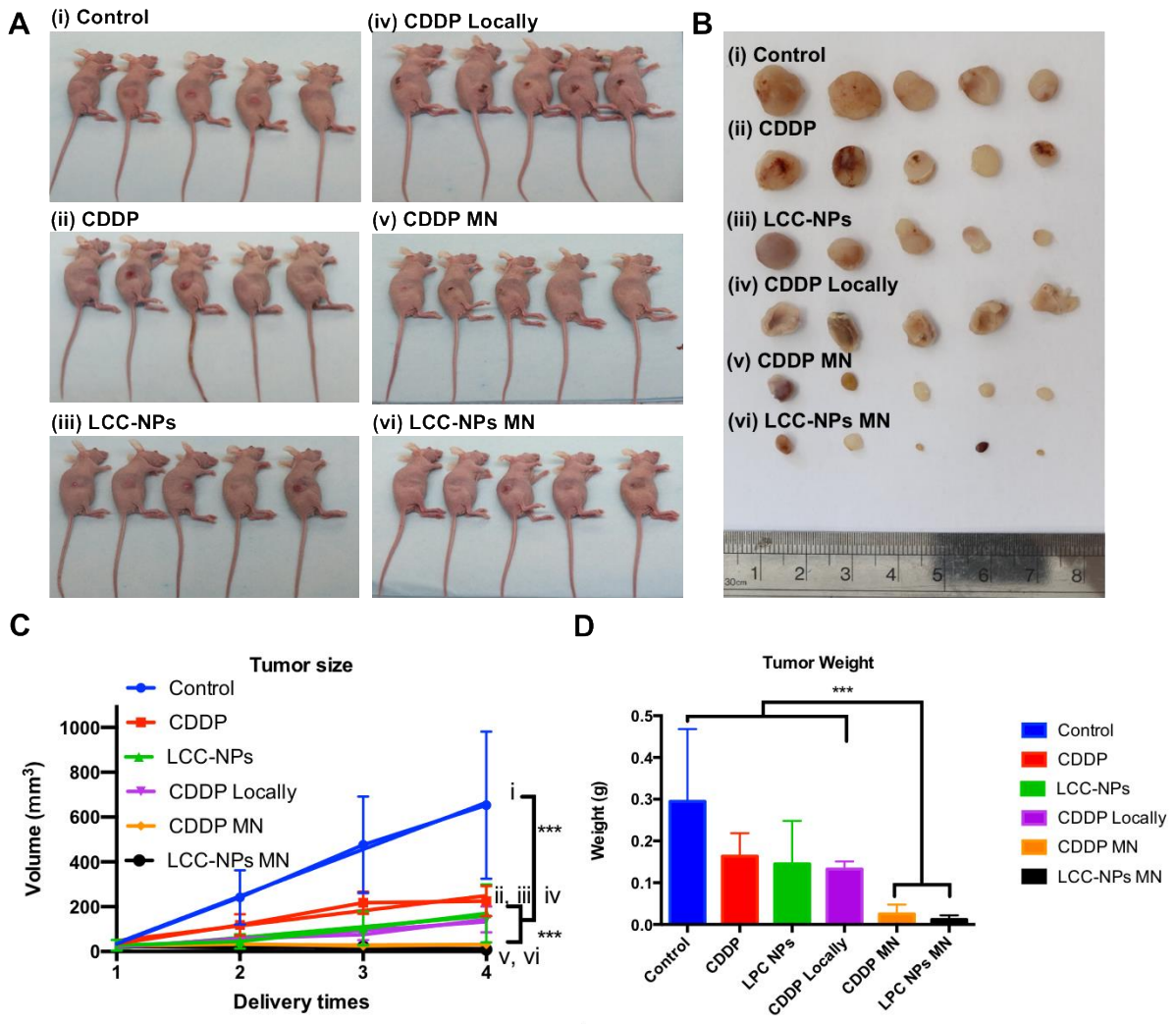

Figure 4. Antitumor efficiency of different groups. (A) Photograph of mice before sacrifice and (B) Tumors harvested in each group: (i. control, ii. CDDP, iii. LCC-NPs, iv. CDDP Locally, v. CDDP MNs, vi. LCC-NPs MNs); (C) Tumor volume of each group at 4 time points (1, 2, and 3 represent times of each injection; 4 represents 3 days after the third injection), (D) Tumor weight of each group: Each bar represents mean ± SD (n = 5); analysis of variance was calculated using the Mann–Whitney U test; *** $p < 0.05$.

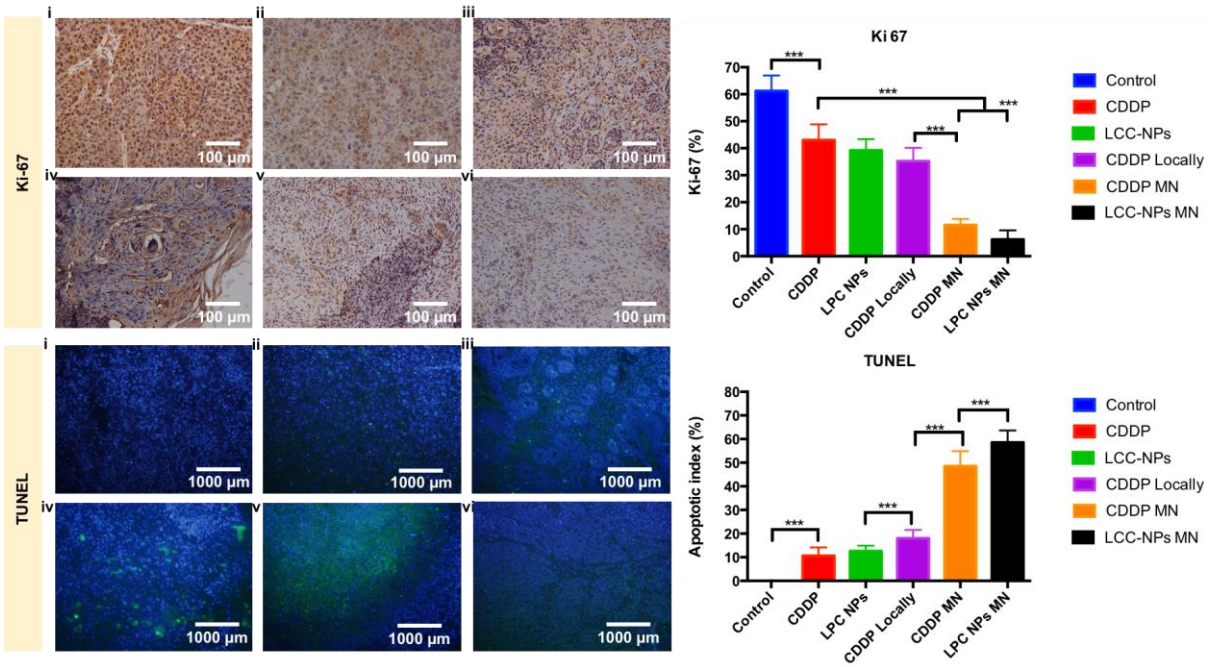

Figure 5. Ki-67 IHC and TUNEL assay in tumor tissues of each group. (i. control, ii. CDDP, iii. LCC-NPs, iv. CDDP Locally, v. CDDP MNs, vi. LCC-NPs MNs): Ki-67 positive cells were stained in brown; Ki-67 density was calculated as positive area/total area. For TUNEL images, green cells were TUNEL-positive; apoptotic index calculated as green cell number/total cell number. Each bar represents mean ± SD (n = 5); analysis of variance was calculated using the Mann–Whitney U test; *** $p < 0.05$.

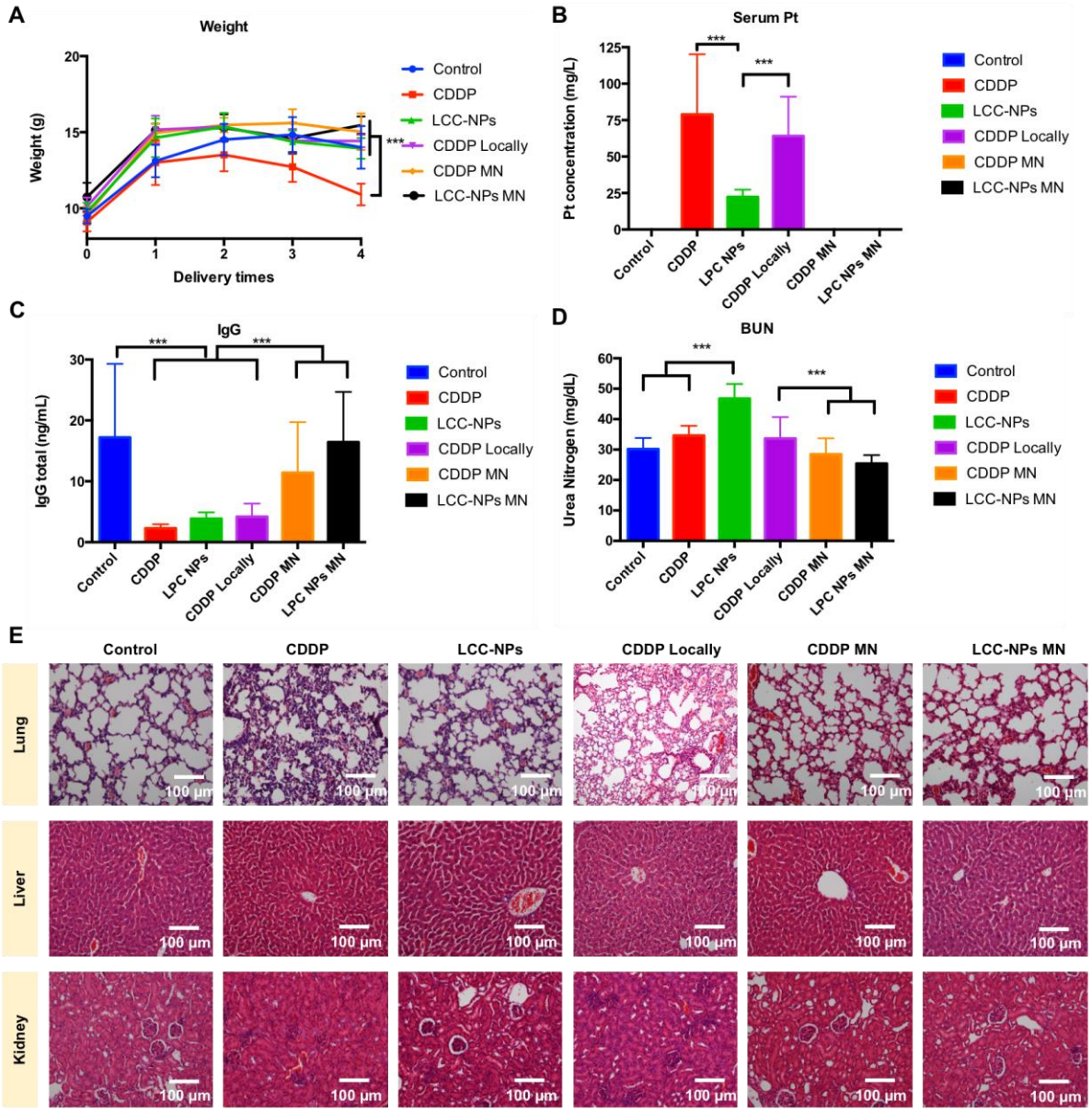

Figure 6. Systemic effects in each group. (A) Body weight of mice in each group (n = 5) after 3 injections: 0 represent the starting point of the experiment; 1, 2, and 3 represent times of each injection; 4 represents 3 days after the third injection; (B) Pt concentration in serum of each mouse before sacrifice; (C) Serum total IgG determined using mouse IgG ELISA kit; (D) BUN level of each group: Data are expressed as mean ± SD (n = 5); analysis of variance was calculated using the Mann–Whitney U test; *** $p < 0.05$; (E) H&E staining of main organs (lung, liver, and kidney) in each group: Intravenous CDDP and locally injected CDDP groups

exhibited severe damage to organs; LCC-NPs groups exhibited mild damage to the liver; MN groups did not show significant pulmonary toxicity, hepatotoxicity, or nephrotoxicity.

Table 1. BUN level of each groups

Group	Mean	Standard derivation
Control	30.1785	3.64682
CDDP	34.6170	3.19778
LCC-NPs	46.7995	4.79354
CDDP Locally	33.6710	7.01871
CDDP MN	28.4625	5.26508
LCC-NPs MN	25.4045	2.76750

Normal range: 12-33 mg/L

References

1. Jemal, A.; Bray, F.; Center, M. M.; Ferlay, J.; Ward, E.; Forman, D., Global Cancer Statistics. *CA: A Cancer Journal for Clinicians* **2011,** *61* (2), 69-90.

2. Dasari, S.; Tchounwou, P. B., Cisplatin in Cancer Therapy: Molecular Mechanisms of Action. *European journal of pharmacology* **2014,** *0*, 364-378.

3. Guo, S.; Huang, L., Nanoparticles Containing Insoluble Drug for Cancer Therapy. *Biotechnol Adv* **2014,** *32* (4), 778-788.

4. Ji, J.; Zuo, P.; Wang, Y. L., Enhanced Antiproliferative Effect of Carboplatin in Cervical Cancer Cells Utilizing Folate-Grafted Polymeric Nanoparticles. *Nanoscale Res Lett* **2015,** *10* (1), 453.

5. He, Z.; Huang, J.; Xu, Y.; Zhang, X.; Teng, Y.; Huang, C.; Wu, Y.; Zhang, X.; Zhang, H.; Sun, W., Co-delivery of Cisplatin and Paclitaxel by Folic Acid Conjugated Amphiphilic PEG-PLGA Copolymer Nanoparticles for the Treatment of Non-small Lung Cancer. *Oncotarget* **2015,** *6* (39), 42150-42168.

6. Ravera, M.; Perin, E.; Gabano, E.; Zanellato, I.; Panzarasa, G.; Sparnacci, K.; Laus, M.; Osella, D., Functional Fluorescent Nonporous Silica Nanoparticles as Carriers for Pt(IV) Anticancer Prodrugs. *J Inorg Biochem* **2015,** *151*, 132-142.

7. Irby, D.; Du, C.; Li, F., Lipid–Drug Conjugate for Enhancing Drug Delivery. *Mol Pharm* **2017,** *14* (5), 1325-1338.

8. Nascimento, A. V.; Singh, A.; Bousbaa, H.; Ferreira, D.; Sarmento, B.; Amiji, M. M., Combinatorial-Designed Epidermal Growth Factor Receptor-Targeted Chitosan Nanoparticles for Encapsulation and Delivery of Lipid-Modified Platinum Derivatives in Wild-Type and Resistant Non-Small-Cell Lung Cancer Cells. *Mol Pharm* **2015,** *12* (12), 4466-4477.

9. Cao, Z. T.; Chen, Z. Y.; Sun, C. Y.; Li, H. J.; Wang, H. X.; Cheng, Q. Q.; Zuo, Z. Q.; Wang, J. L.; Liu, Y. Z.; Wang, Y. C.; Wang, J., Overcoming Tumor Resistance to Cisplatin by Cationic Lipid-assisted Prodrug Nanoparticles. *Biomaterials* **2016,** *94*, 9-19.

10. Guo, S.; Wang, Y.; Miao, L.; Xu, Z.; Lin, C. H.; Huang, L., Turning A Water and Oil Insoluble Cisplatin Derivative Into A Nanoparticle Formulation for Cancer Therapy. *Biomaterials* **2014,** *35* (26), 7647-7653.

11. Girma, W. M.; Tzing, S. H.; Tseng, P. J.; Huang, C. C., Synthesis of Cisplatin(IV) Prodrug-Tethered CuFeS2 Nanoparticles in Tumor-Targeted Chemotherapy and Photothermal Therapy. *ACS Appl Mater Interfaces* **2018,** *10* (5), 4590-4602.

12. Ma, Y.; Boese, S. E.; Luo, Z.; Nitin, N.; Gill, H. S., Drug Coated Microneedles for Minimally-invasive Treatment of Oral Carcinomas: Development and In Vitro Evaluation. *Biomed Microdevices* **2015,** *17* (2), 44.

13. Larraneta, E.; McCrudden, M. T.; Courtenay, A. J.; Donnelly, R. F., Microneedles: A New Frontier in Nanomedicine Delivery. *Pharm Res* **2016,** *33* (5), 1055-1573.

14. Zhang, Y.; Liu, Q.; Yu, J.; Yu, S.; Wang, J.; Qiang, L.; Gu, Z., Locally Induced Adipose Tissue Browning by Microneedle Patch for Obesity Treatment. *ACS Nano* **2017,** *11* (9), 9223-9230.

15. Kim, Y.-C.; Park, J.-H.; Prausnitz, M. R., Microneedles for Drug and Vaccine Delivery. *Advanced Drug Delivery Reviews* **2012,** *64* (14), 1547-1568.

16. Leeladurga, V.; Teja, U. C.; Sultana, S. K.; Sudeep, K.; Anusha, V. S.; Han, T.; Nalluri, B. N.; Das, D. B., Application of Microneedle Arrays for Enhancement of Transdermal Permeation of Insulin: In Vitro Experiments, Scaling Analyses and Numerical Simulations. *AAPS PharmSciTech* **2015**, 915-922.

17. Ling, M. H.; Chen, M. C., Dissolving Polymer Microneedle Patches for Rapid and Efficient Transdermal Delivery of Insulin to Diabetic Rats. *Acta Biomater* **2013,** *9* (11), 8952-8961.

18. Liu, S.; Jin, M. N.; Quan, Y. S.; Kamiyama, F.; Katsumi, H.; Sakane, T.; Yamamoto, A., The Development and Characteristics of Novel Microneedle Arrays Fabricated from Hyaluronic Acid, and Their Application in the Transdermal Delivery of Insulin. *J Control Release* **2012,** *161* (3), 933-941.

19. Yu, J.; Zhang, Y.; Ye, Y.; DiSanto, R.; Sun, W.; Ranson, D.; Ligler, F. S.; Buse, J. B.; Gu, Z., Microneedle-array Patches Loaded with Hypoxia-sensitive Vesicles Provide Fast Glucose-responsive Insulin Delivery. *Proceedings of the National Academy of Sciences* **2015,** *112* (27), 8260.

20. Zhang, Y.; Feng, P.; Yu, J.; Yang, J.; Zhao, J.; Wang, J.; Shen, Q.; Gu, Z., ROS-Responsive Microneedle Patch for Acne Vulgaris Treatment. *ADVANCED THERAPEUTICS* **2018,** *1* (3), 1800035.

21. Chen, M. C.; Lin, Z. W.; Ling, M. H., Near-Infrared Light-Activatable Microneedle System for Treating Superficial Tumors by Combination of Chemotherapy and Photothermal Therapy. *ACS Nano* **2016,** *10* (1), 93-101.

22. Hao, Y.; Dong, M.; Zhang, T.; Peng, J.; Jia, Y.; Cao, Y.; Qian, Z., Novel Approach of Using Near-Infrared Responsive PEGylated Gold Nanorod Coated Poly(L-lactide) Microneedles to Enhance the Antitumor Efficiency of Docetaxel-Loaded MPEG-PDLLA Micelles for Treating an A431 Tumor. *ACS Appl Mater Interfaces* **2017,** *9* (18), 15317-15327.

23. Xu, J.; Xu, B.; Tao, J.; Yang, Y.; Hu, Y.; Huang, Y., Microneedle-Assisted, DC-Targeted Codelivery of pTRP-2 and Adjuvant of Paclitaxel for Transcutaneous Immunotherapy. *Small* **2017,** *13* (28), 1-13.

24. Ye, Y.; Wang, J.; Hu, Q.; Hochu, G. M.; Xin, H.; Wang, C.; Gu, Z., Synergistic Transcutaneous Immunotherapy Enhances Antitumor Immune Responses Through Delivery of Checkpoint Inhibitors. *ACS Nano* **2016,** *10* (9), 8956-8963.

25. Wang, C.; Ye, Y.; Hochu, G. M.; Sadeghifar, H.; Gu, Z., Enhanced Cancer Immunotherapy by Microneedle Patch-Assisted Delivery of Anti-PD1 Antibody. *Nano Letters* **2016,** *16* (4), 2334-2340.

26. Radwan, A. A.; Alanazi, F. K., Targeting Cancer Using Cholesterol Conjugates. *Saudi Pharmaceutical Journal* **2014,** *22* (1), 3-16.

27. Nakagawa, O.; Ming, X.; Huang, L.; Juliano, R. L., Targeted Intracellular Delivery of Antisense Oligonucleotides via Conjugation with Small-Molecule Ligands. *Journal of the American Chemical Society* **2010,** *132* (26), 8848-8849.

28. Qiao, W.; Lan, X.; Tsoi, J. K. H.; Chen, Z.; Su, R. Y. X.; Yeung, K. K.; Matinlinna, J. P., Biomimetic Hollow Mesoporous Hydroxyapatite Microsphere with Controlled Morphology, Entrapment Efficiency and Degradability for Cancer Therapy. *RSC Advances* **2017,** *7* (71), 44788-44798.

29. Baro, M.; de Llobet, L. I.; Figueras, A.; Skvortsova, I.; Mesia, R.; Balart, J., Dasatinib Worsens the Effect of Cetuximab in Combination with Fractionated Radiotherapy in FaDu and A431-derived Xenografted Tumours. *British Journal Of Cancer* **2014,** *111*, 1310.

30. Yang, M.-H.; Wu, M.-Z.; Chiou, S.-H.; Chen, P.-M.; Chang, S.-Y.; Liu, C.-J.; Teng, S.-C.; Wu, K.-J., Direct regulation of TWIST by HIF-1α promotes metastasis. *Nature Cell Biology* **2008,** *10*, 295.

31. Martin, L.; Senesse, P.; Gioulbasanis, I.; Antoun, S.; Bozzetti, F.; Deans, C.; Strasser, F.; Thoresen, L.; Jagoe, R. T.; Chasen, M.; Lundholm, K.; Bosaeus, I.; Fearon, K. H.; Baracos, V. E., Diagnostic Criteria for the Classification of Cancer-associated Weight Loss. *J Clin Oncol* **2015,** *33* (1), 90-99.

32. Solheim, T. S.; Blum, D.; Fayers, P. M.; Hjermstad, M. J.; Stene, G. B.; Strasser, F.; Kaasa, S., Weight Loss, Appetite Loss and Food Intake in Cancer Patients with Cancer Cachexia: Three Peas in A Pod? - Analysis From A Multicenter Cross Sectional Study. *Acta Oncol* **2014,** *53* (4), 539-546.

33. Ghadjar, P.; Hayoz, S.; Zimmermann, F.; Bodis, S.; Kaul, D.; Badakhshi, H.; Bernier, J.; Studer, G.; Plasswilm, L.; Budach, V.; Aebersold, D. M., Impact of Weight Loss on Survival After Chemoradiation for Locally Advanced Head and Neck Cancer: Secondary Results of A Randomized Phase III Trial (SAKK 10/94). *Radiat Oncol* **2015,** *10*, 21.

34. Guo, S.; Wang, Y.; Miao, L.; Xu, Z.; Lin, C. M.; Zhang, Y.; Huang, L., Lipid-coated Cisplatin Nanoparticles Induce Neighboring Effect and Exhibit Enhanced Anticancer Efficacy. *ACS Nano* **2013,** *7* (11), 9896-9904.

Supporting Information

Cell apoptosis and cell cycle arrest induced by LCC-NPs in CAL 27 and SCC 15 cells, and the solubility, stability and cytotoxicity of MNs.

Graphic Abstract

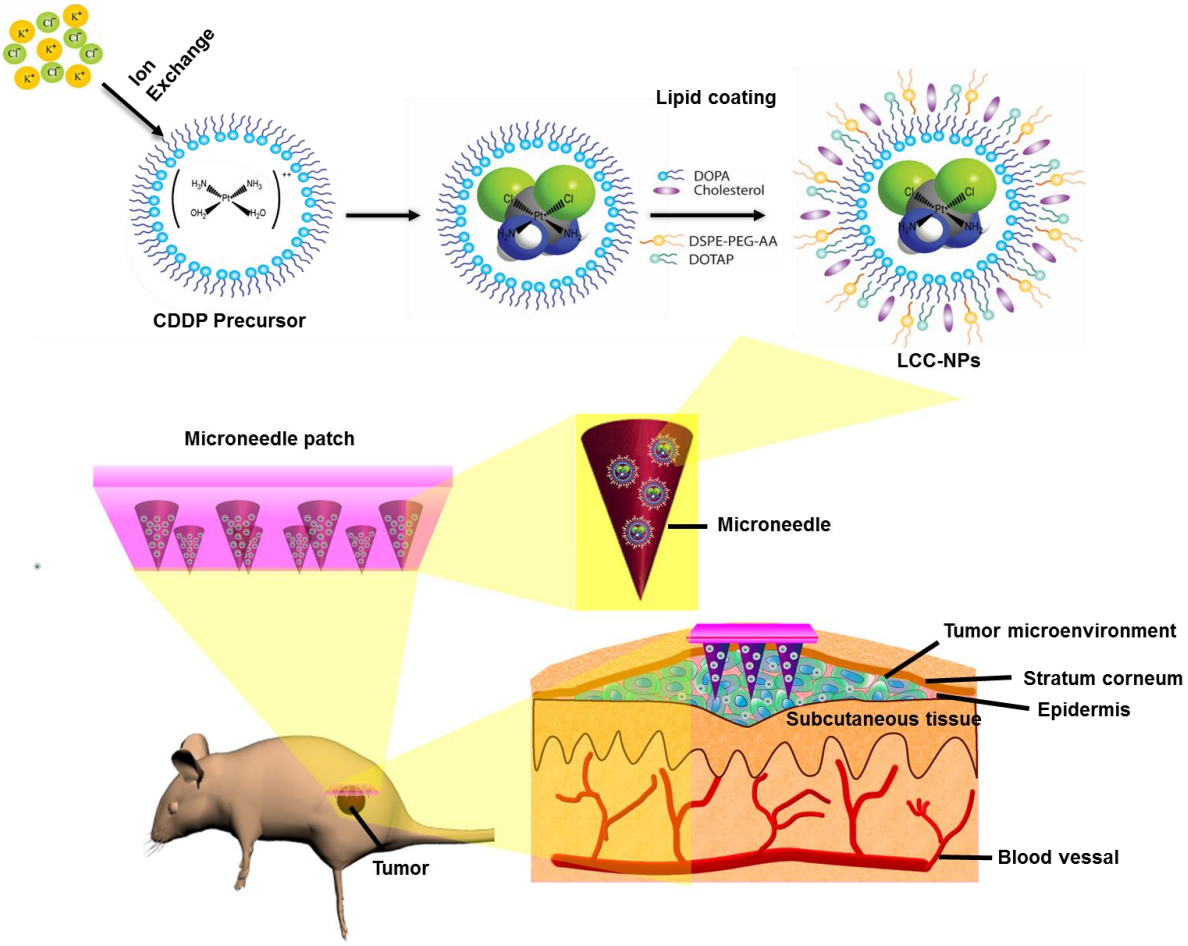

Supporting information

Microneedle-Mediated Delivery of Lipid-Coated Cisplatin Nanoparticles for Efficient and Safe Cancer Therapy

Xinmiao Lan[1], Juncong She[2], Di-an Lin[2], Yu Xu[3], Xuan Li[4], Wei-fa Yang[1], Vivian Wai Yan Lui[5], Lijian Jin[4], Xi Xie[2,6], Yu-xiong Su[1,*]*

1. Discipline of Oral and Maxillofacial Surgery, Faculty of Dentistry, The University of Hong Kong, Hong Kong SAR, China
2. State Key Laboratory of Optoelectronic Materials and Technologies, School of Electronics and Information Technology; Guangdong Province Key Laboratory of Display Material and Technology, Sun Yat-Sen University, Guangzhou, China
3. School of Chinese Medicine, Li Ka Shing Faculty of Medicine, The University of Hong Kong, Hong Kong SAR, China
4. Discipline of Periodontology, Faculty of Dentistry, The University of Hong Kong, Hong Kong SAR, China
5. School of Biomedical Sciences, Faculty of Medicine, The Chinese University of Hong Kong, Hong Kong S.A.R., China
6. The First Affiliated Hospital of Sun Yat-Sen University, Guangzhou, China

[*]Corresponding author

Email: Yu-xiong Su: richsu@hku.hk; Xi Xie: xiexi27@mail.sysu.edu.cn

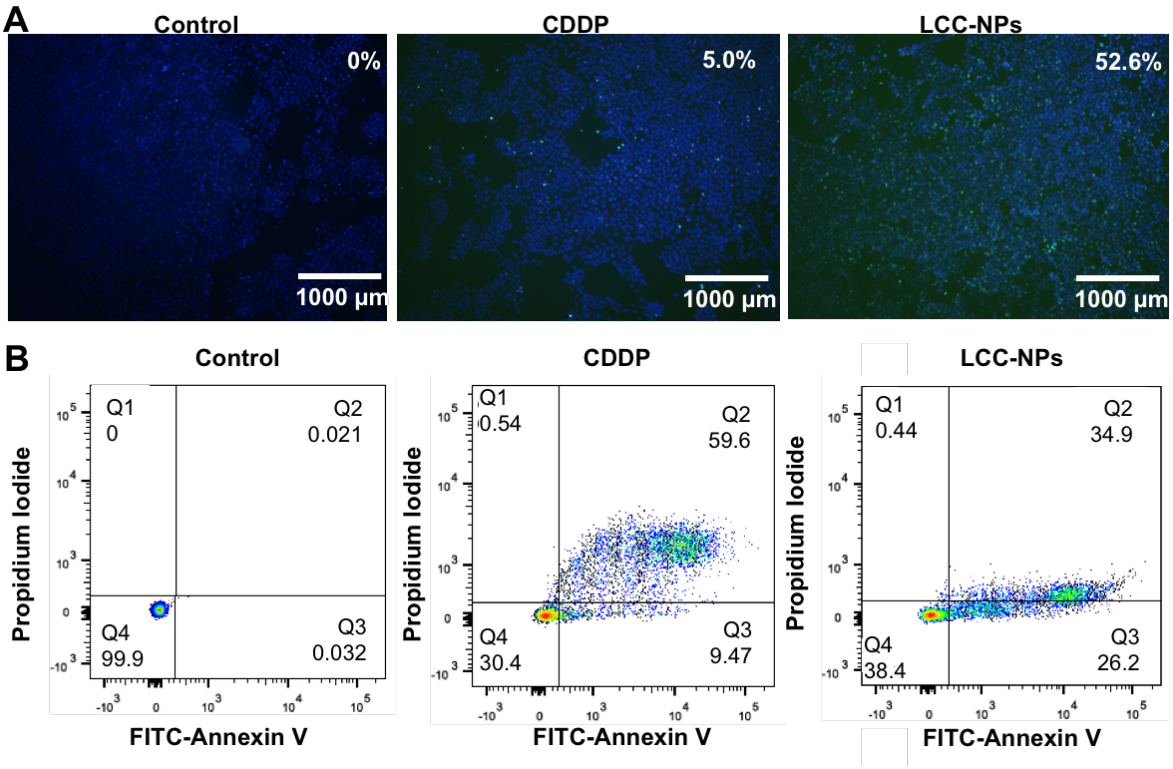

Figure S1. (A) After the treatment of CDDP or LCC-NPs for 4 h, the apoptotic DNA fragmentation in the treated CAL 27 cells were studied using *in situ* TUNEL assay followed by fluorescent imaging (B) CAL 27 cells were stained with annexin V conjugated FITC and PI. The cell apoptosis was analyzed using flow cytometry.

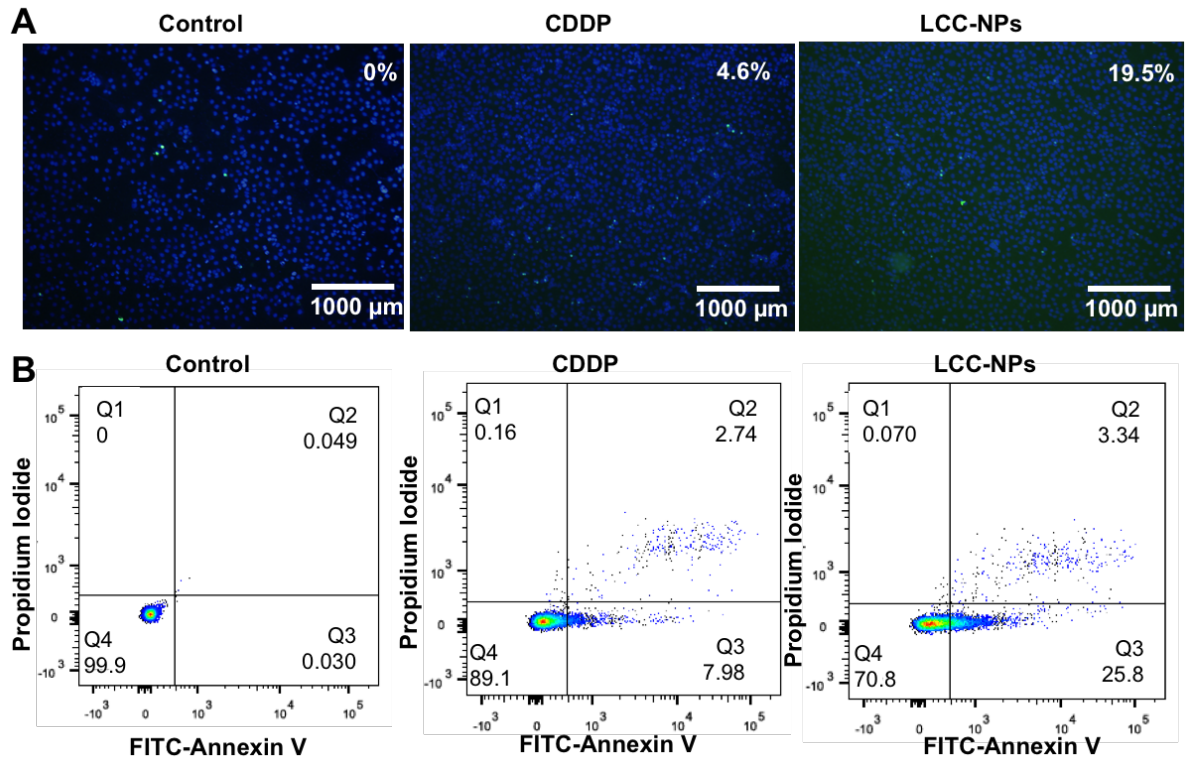

Figure S2. (A) After the treatment of CDDP or LCC-NPs for 4 h, the apoptotic DNA fragmentation in the treated SCC 15 cells were studied using *in situ* TUNEL assay followed by fluorescent imaging (B) SCC 15 cells were stained with annexin V conjugated FITC and PI. The cell apoptosis was analyzed using flow cytometry.

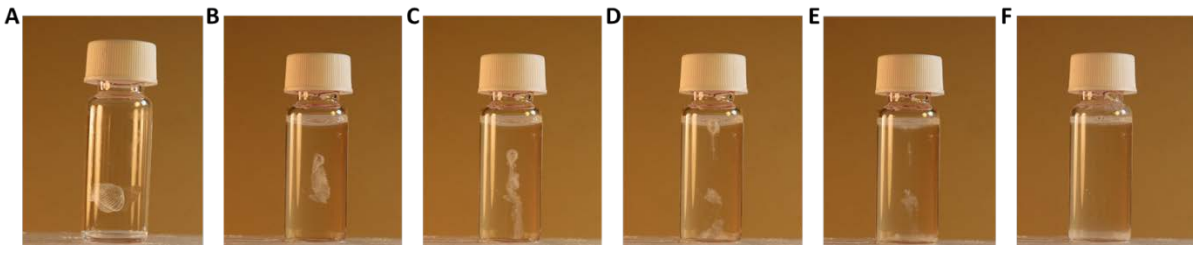

Figure S3. Dissolving process of SCMC material in water (A. Starting point; B. 5s; C. 30s; D. 1min; E. 3min; F. 5min).

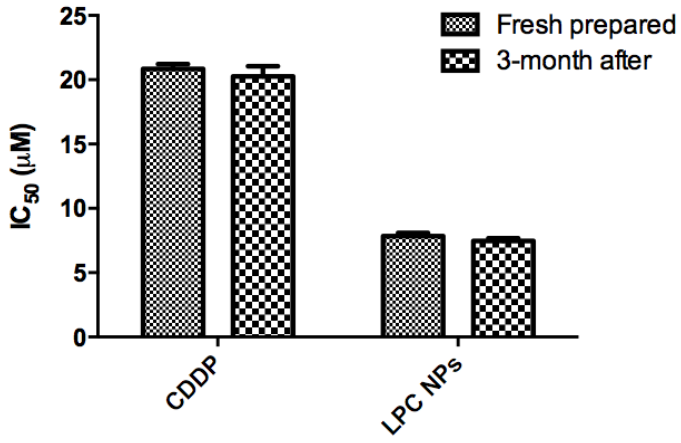

Figure S4. IC_{50} value of CDDP and LCC-NPs 3 months after prepared compared with the fresh prepared drugs on CAL 27 cell line. No significant difference was detected.

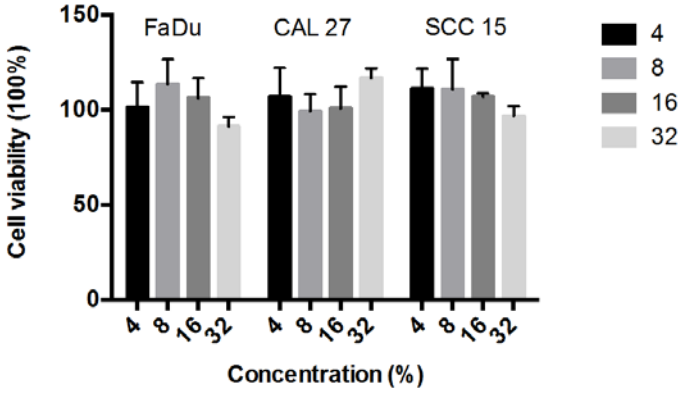

Figure S5. Cell viability of three HNSCC cell lines when treated with different concentration of SCMC.